Check for updates

AGU ADVANCING EARTH AND SPACE SCIENCES

Geophysical Research Letters

RESEARCH LETTER
10.1029/2025GL120206

Influence of Tibetan Plateau Snow Cover on ENSO Variability via the Dust-Iron Fertilization

Chao Zhang[1,2], Anmin Duan[1], Thomas J. Browning[2], Yuxin Xie[1], and Eric P. Achterberg[2]

[1]Center for Marine Meteorology and Climate Change, State Key Laboratory of Marine Environmental Science, College of Ocean and Earth Sciences, Xiamen University, Xiamen, China, [2]Marine Biogeochemistry Division, GEOMAR Helmholtz Centre for Ocean Research Kiel, Kiel, Germany

Key Points:

- Tibetan Plateau snow cover (TPSC) contributes one-quarter of El Niño–Southern Oscillation (ENSO) variability
- Documenting the biogeochemical mechanism of ENSO formation
- A dust-iron fertilization pathway links reduced TPSC to La Niña development

Supporting Information:

Supporting Information may be found in the online version of this article.

Correspondence to:

C. Zhang and A. Duan,
chaozhang@xmu.edu.cn;
amduan@xmu.edu.cn

Citation:

Zhang, C., Duan, A., Browning, T. J., Xie, Y., & Achterberg, E. P. (2026). Influence of Tibetan Plateau snow cover on ENSO variability via the dust-iron fertilization. *Geophysical Research Letters*, *53*, e2025GL120206. https://doi.org/10.1029/2025GL120206

Received 22 OCT 2025
Accepted 26 FEB 2026

Author Contributions:

Conceptualization: Chao Zhang
Data curation: Chao Zhang, Yuxin Xie
Formal analysis: Chao Zhang, Thomas J. Browning, Eric P. Achterberg
Funding acquisition: Anmin Duan
Investigation: Chao Zhang, Anmin Duan, Thomas J. Browning, Eric P. Achterberg
Methodology: Chao Zhang, Thomas J. Browning
Project administration: Chao Zhang, Anmin Duan
Resources: Chao Zhang, Yuxin Xie, Eric P. Achterberg
Software: Chao Zhang, Yuxin Xie
Supervision: Anmin Duan, Eric P. Achterberg
Validation: Chao Zhang, Yuxin Xie
Visualization: Chao Zhang

© 2026. The Author(s).
This is an open access article under the terms of the Creative Commons Attribution-NonCommercial-NoDerivs License, which permits use and distribution in any medium, provided the original work is properly cited, the use is non-commercial and no modifications or adaptations are made.

Abstract The El Niño–Southern Oscillation (ENSO) and Tibetan Plateau, as key drivers of Earth's climate system, exert bidirectional controls that complicate causal attribution. Here, we integrate satellite-derived Tibetan Plateau snow cover (TPSC) with causal inference to establish TPSC-ENSO conversion factor. Using this factor, we estimate that TPSC anomalies contribute 24.8% (6.4%–44.1%) of September ENSO variability. Notably, TPSC-modulated biogeochemical processes are as influential as equatorial zonal wind mechanisms, constituting an additional ENSO driver. Reduced TPSC intensifies the Tibetan Plateau heat source, driving ascendant easterly anomalies. This accelerates the tropical easterly jet, transporting more Saharan dust to the tropical Pacific. Dust-iron fertilization stimulates phytoplankton accumulation across iron-limited central-eastern Equatorial Pacific, reducing solar irradiance penetration depth, lowering upper ocean heat content by 21% (7%–29%), and promoting La Niña development. Conversely, high TPSC favors El Niño development. These findings quantify TPSC's impact on ENSO variability, unveiling a biogeochemical pathway linking dust-iron fertilization to ocean energetics.

Plain Language Summary The El Niño–Southern Oscillation (ENSO) is a known modulator of global climate anomalies, including variations in Tibetan Plateau snow cover (TPSC). However, whether TPSC, acting as a hemispheric-scale climate factor, influences ENSO occurrence has remained unclear. This study reveals how Tibetan Plateau snow cover (TPSC) affects ENSO. We show that reduced snow on the Tibetan Plateau acts as a heat source, triggering a cascade of effects: it alters wind patterns, leading to increased transport of Saharan dust to the iron limited Pacific Ocean. Iron from the dust fertilizes phytoplankton growth that shades the ocean surface, reducing solar heat absorption and ultimately promoting the development of La Niña conditions. This identified biogeochemical pathway provides a fresh perspective on ENSO dynamics.

1. Introduction

Climate system internal variability is crucial in driving Earth's atmospheric and oceanic variations. ENSO, a dominant ocean-atmosphere interaction driver (Scaife et al., 2024; Tziperman et al., 1994; Zhao et al., 2024), and the Tibetan Plateau, a key land-atmosphere modulator (Huang et al., 2023; Wu et al., 2014), constitute essential component of this variability. Both have profound impacts on global climate, ecosystems, and socio-economic systems (Wen et al., 2020; Wu et al., 2024). Nevertheless, their complex bidirectional interactions complicate causal attribution, hinder realistic contribution quantification (Henderson et al., 2018), and constrain understanding of Earth's climate mechanisms.

Modern and paleoclimate records, alongside model evidence, illustrate ENSO's influences on the Tibetan Plateau climate systems. The associated pathways include atmospheric teleconnections (Jiang et al., 2019; Shaman & Tziperman, 2005), Walker circulation shifts (Wang et al., 2024), and altered local circulation (Wu et al., 2024). El Niño enhances eastern Plateau winter snowfall and summer precipitation through atmospheric waves and anomalous cyclones (Jiang et al., 2019), and reducing Plateau ozone via South Asian High intensification (Li et al., 2023). Paleoclimate evidence from lake sediments, ice cores, and tree rings further indicates that positive ENSO phases increase Plateau lake levels and precipitation (Li et al., 2022; Wu et al., 2024).

In contrast, only one terrain model experiment (Wen et al., 2020) and a surface winds study (Yu et al., 2022) have examined the Tibetan Plateau's impact on ENSO variability. Observations and simulations reveal that reduced Plateau heating induces eastward-propagating atmospheric waves, generating a tropical eastern Pacific low-pressure anomaly (Yu et al., 2022). This anomaly elevates sea surface temperature (SST) in the central and

Writing – original draft: Chao Zhang
Writing – review & editing: Anmin Duan, Thomas J. Browning, Eric P. Achterberg

eastern Equatorial Pacific by weakening trade winds. Thus, while ENSO's influence on the Tibetan Plateau is well documented, mechanisms underlying the Plateau's impact on ENSO variability remain poorly understood.

Both Tibetan Plateau snow cover (TPSC) and surface sensible heat constitute important thermal drivers of global climate variations (Li et al., 2018; C. Zhang et al., 2021). Compared to sensible heat, TPSC exhibits both cross-seasonal impacts and predictive potential attributable to persistent memory of snow anomalies (Wu et al., 2011; C. Zhang et al., 2023). Although hemispheric-scale atmospheric waviness mechanisms have been proposed (Wu et al., 2011; C. Zhang et al., 2025), a well-established causal chain linking TPSC, atmospheric circulation, and ENSO is still lacking. This absence hinders the precise quantification of TPSC's contribution to ENSO and obscures underlying mechanisms. We therefore integrate satellite observations, model simulations, and causality analysis to establish an impact conversion factor for TPSC-ENSO contribution quantification. Unlike prior wind-evaporation-SST feedback mechanism (Wen et al., 2020; Yu et al., 2022, 2023), we propose a novel biogeochemical mechanism to explain how TPSC influences ENSO. In the following, Section 2 describes data, model experiments, and causality technique. The results are presented in Section 3, followed by the conclusions and discussions in final section.

2. Data and Methods

2.1. Data

Briefly, data sets used include (see Supporting Information S1 for details): National Oceanic and Atmospheric Administration (NOAA) satellite snow cover (1979–2021) (Robinson et al., 2012), validated against National Snow and Ice Data Center (NSIDC) snow cover, Big Earth Data Platform snow depth, and ERA5 snowfall for Tibetan Plateau accuracy (C. Zhang & Jia, 2022; C. Zhang et al., 2023). MODIS satellite Level-3 chlorophyll-*a* concentration data derived from the Global Ocean Color. Second Modern-Era Retrospective analysis for Research and Applications (MERRA-2) dust concentrations (Global Modeling and Assimilation Office (GMAO), 2015. ORAS5 ocean heat content and mixed layer depth (Zuo et al., 2018). ERA5 (Hersbach et al., 2020) and NCEP/DOE-R2 (Kanamitsu et al., 2002) atmospheric reanalysis. Hadley Center SST (HadISST) (Rayner et al., 2003). Seawater dissolved iron concentration from the Mercator-Ocean NEMO-PISCES model (Global Ocean Biogeochemistry Hindcast, 2024).

2.2. The Conversion Factor Derived From Causality Analysis

A bidirectional relationship exists between TPSC and ENSO. To verify their causality, we applied the Liang–Kleeman information flow (LKIF) method (Liang & Kleeman, 2005). This approach is rigorously derived from first principles and information theory, enabling quantitative causality measurement between variables (Liang, 2016; Liang & Kleeman, 2005). Consequently, LKIF-determined causation constitutes a fundamental physical concept. This method has been successfully applied cross disciplines including: climate-driven phytoplankton identification, long-term ENSO projections, CO_2-global warming relationships, origins of polar sea-ice, and von Neuman entropy in quantum systems (Li et al., 2024; Yi & Bose, 2022; C. Zhang et al., 2025). The LKIF framework is structured as follows (Liang, 2016; Liang & Kleeman, 2005):

$$\dot{x}_{j,n} = \frac{x_{j,n+k} - x_{j,n}}{k\Delta t} \tag{1}$$

$$C_{ij} = \overline{(x_i - \overline{x_i})(x_j - \overline{x_j})} \tag{2}$$

$$\hat{T}_{2\to 1} = \frac{C_{11}C_{12}C_{2,d1} - C_{12}^2 C_{1,d1}}{C_{11}^2 C_{22} - C_{11}C_{12}^2} \tag{3}$$

where $\hat{T}_{2\to 1}$ represents the information flow from variable x_2 (e.g., TPSC) to x_1 (e.g., ENSO). C_{ij} denotes the covariance matrix, while $\dot{x}_{j,n}$ refers to the Euler forward differencing scheme. The term $C_{i,dj}$ indicates the covariance between the differencing scheme and variable x_i. Δt refers to their time step. Causality is determined as: When $\hat{T}_{2\to 1} \neq 0$ and statistically significant, changes in x_2 increase the entropy of x_1, indicating that x_2 has a causal impact on x_1. Conversely, $\hat{T}_{2\to 1} = 0$ or non-significance indicates x_2 has no causal impact on x_1.

19448007, 2026, 6, Downloaded from https://agupubs.onlinelibrary.wiley.com/doi/10.1029/2025GL120206 by Chao Zhang - Xiamen University , Wiley Online Library on [14/03/2026]. See the Terms and Conditions (https://onlinelibrary.wiley.com/terms-and-conditions) on Wiley Online Library for rules of use; OA articles are governed by the applicable Creative Commons License

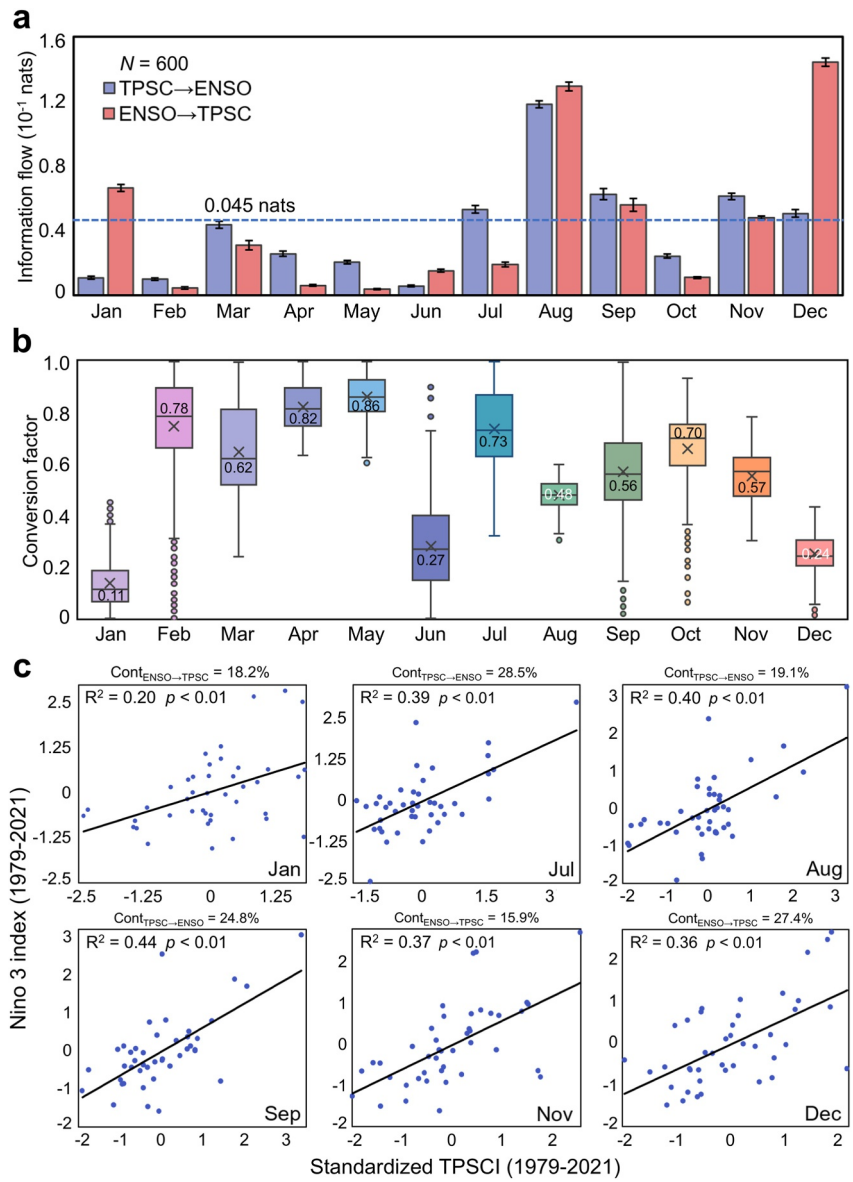

Figure 1. Detecting TPSC-ENSO causal relationships via information flow framework. (a) Monthly area-weighted mean of information flow (1979–2021) between TPSC and SST in the Niño 3 regions. Blue/red bars: information flow from TPSC to ENSO and the reverse flow. Error bars represent 99% confidence intervals across 600 grids within the Niño 3 region. Horizontal line used to select study months. (b) Monthly conversion factor for TPSC's influence on ENSO (1979–2021), calculated as the ratio of information flow from TPSC to ENSO divided by total information flow between TPSC and ENSO. Horizontal line: median. While dots: outliers. (c) Fitted plot shows the relationship between TPSC and Niño 3 indices. $\text{Cont}_{\text{TPSC}\to\text{ENSO}}$ indicates TPSC's contributions to ENSO, whereas $\text{Cont}_{\text{ENSO}\to\text{TPSC}}$ represents ENSO's contributions to TPSC. Details on the calculation of the conversion factor are provided in Figure S4 in Supporting Information S1.

This study derives the conversion factor (Γ) through calculation of information flow from TPSC to ENSO ($\hat{T}_{\text{TPSC}\to\text{ENSO}}$) and their reverse flow ($\hat{T}_{\text{ENSO}\to\text{TPSC}}$):

$$\Gamma = \frac{\hat{T}_{TPSC\to ENSO}}{\hat{T}_{TPSC\to ENSO}+\hat{T}_{ENSO\to TPSC}} \quad (4)$$

19448007, 2026, 6, Downloaded from https://agupubs.onlinelibrary.wiley.com/doi/10.1029/2025GL120206 by Chao Zhang - Xiamen University , Wiley Online Library on [14/03/2026]. See the Terms and Conditions (https://onlinelibrary.wiley.com/terms-and-conditions) on Wiley Online Library for rules of use; OA articles are governed by the applicable Creative Commons License

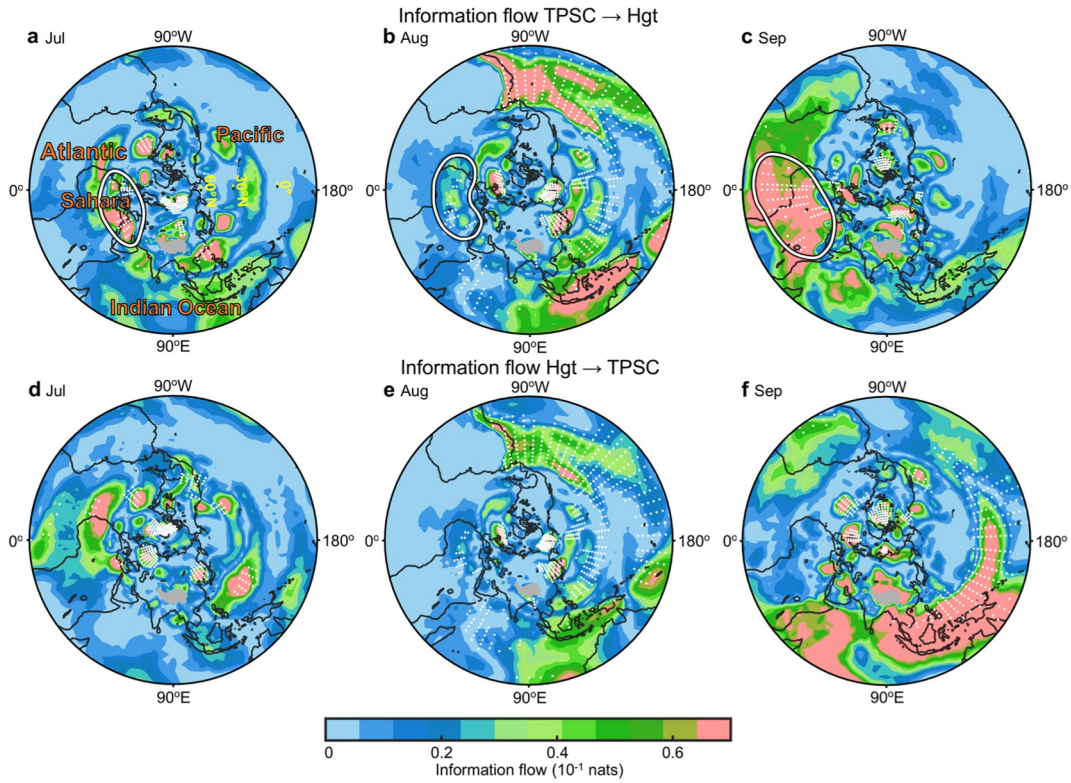

Figure 2. TPSC-atmospheric circulation causality. Information flow from TPSC to ERA5 850 hPa geopotential height in (a) July, (b) August, and (c) September from 1979 to 2021. The circled area indicates significant information flow over the Sahara during July–September, highlighting persistent impacts of TPSC on Saharan atmospheric circulation. (d–f) The reverse information flow from 850 hPa geopotential height to TPSC. Dotted areas represent significant information flow at the 95% level (two-tailed *z*-test).

The conversion factor F quantifies TPSC's causal impact magnitude on ENSO (Figure 1b). Crucially, traditional coefficients of determination (R^2) fail to estimate true contributions due to lack of causality. By applying F, we obtain the realistic TPSC's contributions to ENSO: $\mathsf{F} \times R^2$ (Figure 1c).

2.3. Dust-Derived Dissolved Iron Model

Due to the enhanced solubility of fine versus coarse dust aerosol, we computed dust-derived dissolved iron separately by particle size (Mahowald et al., 2009). The dust-derived soluble iron flux model (Figure 3d) integrates contributions from both fine and coarse fractions:

$$\mathrm{dust}_{\mathrm{Fe}} = f_{\mathrm{Fe}} \times \left(\mathrm{dust}^{\mathrm{fine}}_{\mathrm{surface}} \times \mathrm{velocity}^{\mathrm{vertical}}_{1000\mathrm{hPa}} \times S^{\mathrm{fine}} + \mathrm{dust}^{\mathrm{coarse}}_{\mathrm{surface}} \times \mathrm{velocity}^{\mathrm{vertical}}_{1000\mathrm{hPa}} \times S^{\mathrm{coarse}}\right) \quad (5)$$

$$S^{\mathrm{fine}} = 12\% \times \left[1 + \mathrm{normalized}\left(1/\mathrm{dust}^{\mathrm{fine}}_{\mathrm{surface}}\right)\right] \quad (6)$$

$$S^{\mathrm{coarse}} = 2\% \times \left[1 + \mathrm{normalized}\left(1/\mathrm{dust}^{\mathrm{fine}}_{\mathrm{surface}}\right)\right] \quad (7)$$

where, f_{Fe} (total iron loading in dust aerosols) is set at 3.5% (Luo et al., 2008; Matsui et al., 2018). Surface mass concentration of fine (PM < 2.5) and coarse (PM > 2.5) dust aerosols are denoted as $\mathrm{dust}^{\mathrm{fine}}_{\mathrm{surface}}$ and $\mathrm{dust}^{\mathrm{coarse}}_{\mathrm{surface}}$, respectively. $\mathrm{velocity}^{\mathrm{vertical}}_{1000\mathrm{hPa}}$ denotes vertical velocity at 1,000 hPa. S^{fine} and S^{coarse} indicate iron solubility for fine and coarse dust aerosols, respectively. Global iron solubility defaults are 12% (Mahowald et al., 2018) for fine dust and 2% (Krishnamurthy et al., 2010) for coarse dust, consistent with established ranges (Mahowald et al., 2009; Matsui et al., 2018).

19448007, 2026, 6, Downloaded from https://agupubs.onlinelibrary.wiley.com/doi/10.1029/2025GL120206 by Chao Zhang - Xiamen University , Wiley Online Library on [14/03/2026]. See the Terms and Conditions (https://onlinelibrary.wiley.com/terms-and-conditions) on Wiley Online Library for rules of use; OA articles are governed by the applicable Creative Commons License

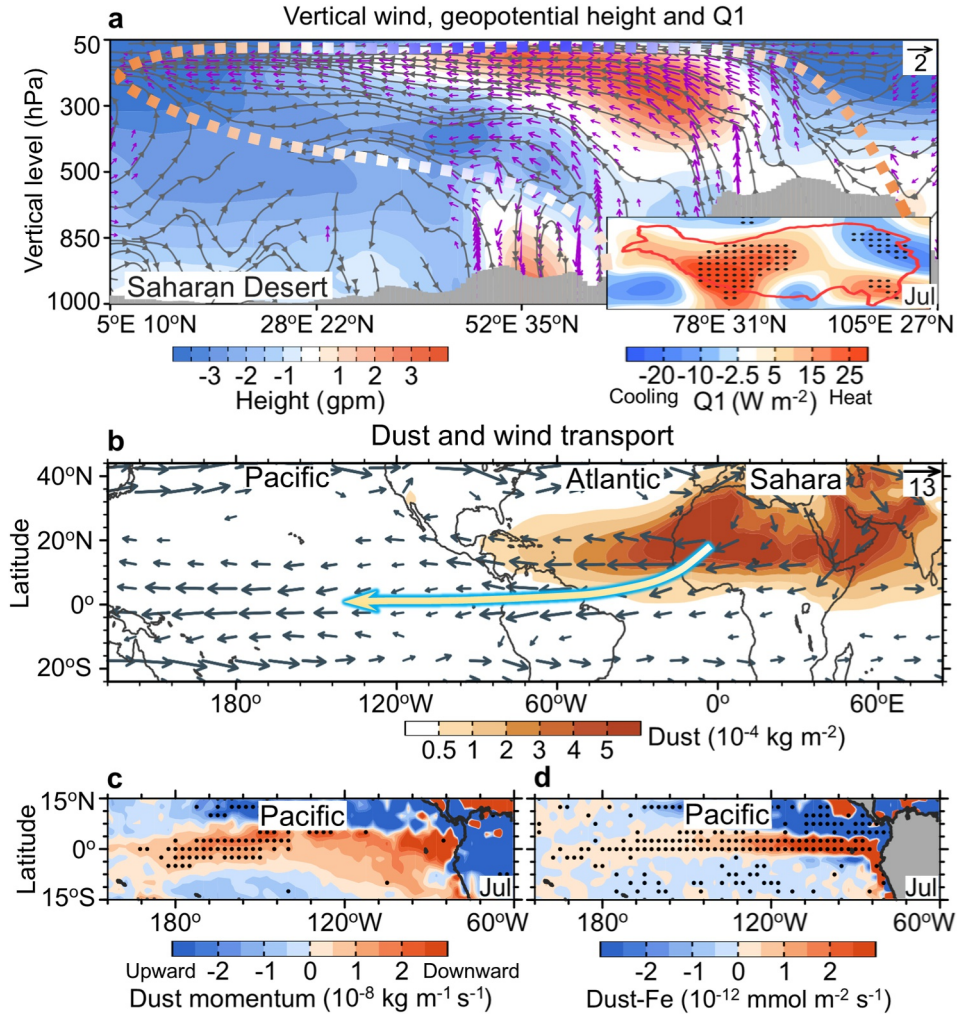

Figure 3. TPSC-modulated Equatorial Pacific dust-iron fertilization. (a) TPSC-associated vertical wind (vectors) and geopotential height (shading) anomalies along Sahara-Plateau (Figure S13 in Supporting Information S1), with insert showing atmospheric cooling/heat source anomalies. Thick line area indicates that when TPSC is low, anomalous Plateau convection propagates to the Saharan Desert. (b) GEOS column dust climatology (shading) with ERA5 500 hPa winds (vectors). Thick yellow arrow outline Sahara-Pacific dust transport pathways (see Figure S13b in Supporting Information S1). (c) Dust momentum (dust concentration × 700 hPa vertical velocity) and (d) dust-derived soluble iron flux anomalies, calculating utilizing the dust-derived iron model (see Methods). All these anomalies are calculated using linear regression onto the -TPSC index. Black dots and purple vectors: 95% statistical significance. All panels: July data (August/September in Figure S10 in Supporting Information S1).

2.4. Ocean Energetic Impacts From Widespread Phytoplankton Blooms

Based on the Beer–Lambert law, penetration depth (H_p) was calculated using satellite-derived chlorophyll data (Figure 4c), as formulated bellow (Murtugudde et al., 2002):

$$H_p(x,y) = \frac{1}{K_p(x,y)} = \frac{1}{K_w + a \cdot \mathrm{Chl}(x,y)^b} \tag{8}$$

where K_p represents the solar radiation attenuation coefficient, and K_w, a, and b are constants with values of 0.0027 m^{-1}, 0.518 mg^{-1} m^2, and 0.428, respectively (Murtugudde et al., 2002).

Changes in the mixed layer depth (H_m) regulate solar radiation distribution between mixed layer and subsurface layer, where large-scale chlorophyll blooms significantly alter solar radiation penetration depth (H_p). Concurrent

19448007, 2026, 6, Downloaded from https://agupubs.onlinelibrary.wiley.com/doi/10.1029/2025GL120206 by Chao Zhang - Xiamen University , Wiley Online Library on [14/03/2026]. See the Terms and Conditions (https://onlinelibrary.wiley.com/terms-and-conditions) on Wiley Online Library for rules of use; OA articles are governed by the applicable Creative Commons License

H_m and H_p modulate oceanic energy balance. Using H_p and H_m, absorbed solar radiation (Q_{abs}) and chlorophyll-induced temperature change rate (R_{temp}) in the mixed layer can be calculated via (R.-H. Zhang, 2015):

$$Q_{\text{abs}}(H_m, H_p) = Q_{\text{sr}}[1 - \gamma \exp(-H_m/H_p)] \tag{9}$$

$$R_{\text{temp}}(Q_{\text{abs}}, H_m) = \frac{Q_{\text{abs}}(H_m, H_p)}{\rho_0 C_p H_m} = \frac{Q_{\text{sr}}[1 - \gamma \exp(-H_m/H_p)]}{\rho_0 c_p H_m} \tag{10}$$

where Q_{sr} refers to surface solar radiation flux. $\gamma = 0.33$ represents the radiation fraction that penetrates beyond the uppermost few centimeters of the sea surface. ρ_0 (1,025 kg m^{-3}) and C_p (3,990 J kg^{-1} K^{-1}) indicate the seawater density and the specific heat capacity, respectively.

2.5. Numerical Experiments

To test the hypothesis that reduced TPSC influences atmospheric circulation via diabatic heating changes, we conducted two sets of numerical experiments (see Supporting Information S1 for details) using Community Earth System Model (CESM, version 1.1.1; Park et al., 2014; Lawrence et al., 2012).

Control Run: A 40-year simulation forced with 1980–2020 SST climatology and the original Tibetan Plateau heat source.

Perturbation Run: A 20-year experiment where the July-September Plateau albedo is reduced by 0.3 (Cohen et al., 2021), representing the diabatic heating forcing associated with TPSC reduction.

The atmospheric response is derived by differencing between the 20-year perturbation experiment and final 10-year control outputs.

2.6. Statistical Analysis

Given the interannual nature of ENSO variability, we focus on this timescale using Gaussian-filtered high-frequency signals (<8-year) across all data sets. Statistical significance is accessed via two-tailed z-test for information flow and Student's t-test for other analysis.

3. Results

3.1. Impact Conversion Factor

To establish TPSC-circulation-ENSO causality, we employ the Liang-Kleeman information flow method, a quantitative causal inference framework measuring information transfer between systems (Liang & Kleeman, 2005; see Methods). Significant TPSC-ENSO information flow occurs in January, July-September, November, and December (Figure 1a), suggesting strong causal connections during these months. To confirm the robustness, we utilize a widely recognized causal analysis framework, PCMCI (see Methods in Supporting Information S1). The PCMCI framework yields consistently strong link coefficients in these periods (Figure S1 in Supporting Information S1), supporting the reliability of the causal connections in identical months.

The bidirectional information flow (TPSC ↔ ENSO) is found in the boreal warm season (August-September), but shifts to unidirectional flow (ENSO → TPSC) that dominates in January and December (Figure 1a). Thus, strong interactions prevail in warm seasons, while ENSO controls TPSC variations in cold seasons. Notably, traditional metrics, such as correlation coefficients, can only qualitatively describe the association between TPSC and ENSO, but cannot quantify the absolute contribution of TPSC → ENSO (or vice versa).

We therefore derive TPSC's impact conversion factor using information flow magnitude, defined as the proportion of information flow magnitude from TPSC relative to the total TPSC-ENSO information flow magnitude (Figure 1b; see Methods). The information flow based conversion factor measures the degree of causal contribution between TPSC and ENSO, with values ranging from 0 to 1, reflecting the extent of TPSC's influence on ENSO. For example, a conversion factor of 0.48 in August indicates near-symmetric bidirectional influence; the January value of 0.11 suggests a dominant ENSO's influence on TPSC.

19448007, 2026, 6, Downloaded from https://agupubs.onlinelibrary.wiley.com/doi/10.1029/2025GL120206 by Chao Zhang - Xiamen University , Wiley Online Library on [14/03/2026]. See the Terms and Conditions (https://onlinelibrary.wiley.com/terms-and-conditions) on Wiley Online Library for rules of use; OA articles are governed by the applicable Creative Commons License

19448007, 2026, 6, Downloaded from https://agupubs.onlinelibrary.wiley.com/doi/10.1029/2025GL120206 by Chao Zhang - Xiamen University , Wiley Online Library on [14/03/2026]. See the Terms and Conditions (https://onlinelibrary.wiley.com/terms-and-conditions) on Wiley Online Library for rules of use; OA articles are governed by the applicable Creative Commons License

Based on the identified months, we assess bidirectional TPSC-ENSO contributions using impact conversion factor. Monthly TPSC indices are constructed by standardizing area-weighted snow cover means over the ENSO related significant domain, and applying interannual timescale filters (Figures S2 and S3 in Supporting Information S1). Using impact conversion factor, we estimate that TPSC contributes 28.5% (July), 19.1% (August), and 24.8% (September) of ENSO variability. In contrast, ENSO modulates TPSC variability by 18.2% (January), 15.9% (November), and 27.4% (December) (all $p < 0.01$; Figure 1c). Boxplot whiskers in Figure 1b represent the full statistical range of values (e.g., TPSC contribution to ENSO: 6.4%–44.1% in September).

3.2. Link TPSC Variations to Pacific Dust-Derived Iron Fertilization

The analysis above reveals a pronounced warm-season causal linkage between TPSC and ENSO. Through lag regression and composite analysis, we further show that a reduced July TPSC is followed by a La Niña-like SST pattern and a dipole structure in the height field (Figures S5–S8 in Supporting Information S1). Given that ENSO events typically intensify in autumn and peak in winter—a self-sustaining seasonal pattern known as phase locking—we present a composite analysis that excludes strong and moderate ENSO years to reduce this inherent influence. The results indicate that a reduced July TPSC is followed by a La Niña-like SST pattern in the subsequent autumn (Figure S7 in Supporting Information S1). After removing moderate ENSO events, the La Niña signal persists (Figure S7b in Supporting Information S1). This implies that the July TPSC may influence the later development of moderate ENSO. These results motivate us to clarify its physical impact pathways.

Surface divergent anomalies, coupled with clear-sky conditions, drive accelerated snowmelt (C. Zhang & Jia, 2022). As such, TPSC-associated significant moisture divergence anomalies during peak snowmelt months (July-August; Figure S8a in Supporting Information S1). This indicates atmospheric control on TPSC melting. Conversely, elevated TPSC is linked to significant moisture source anomalies over the central-western Plateau ($-10\sim-25$ W m^{-2}; Figure S8b in Supporting Information S1), sustained through snowmelt and meltwater evaporation processes (Xiao & Duan, 2016; C. Zhang & Jia, 2022). These moisture source anomalies enhance moisture export from the Tibetan Plateau (Figure S9a in Supporting Information S1), indicating TPSC's regulation of the regional hydrological dynamics during warm seasons.

Based on TPSC-regulated local moisture transport mechanisms, we examine TPSC-driven remote climatic impacts. Previous studies document TPSC impacts on hemisphere-scale climate systems, including the Pacific-North American pattern (Wu et al., 2011), and European and Arctic climate variability (Liu et al., 2022), primarily via eastward-propagating wave trains along the subtropical westerly belt. In essence, the causal impacts of Pacific circulation on TPSC (0.04–0.08 nats; Figures 2d–2f) make it hard to separate TPSC-driven impacts through the eastward pathway. Crucially, TPSC maintains a persistent causal influence on tropical Saharan circulation (0.03–0.07 nats; Figures 2a–2c). This identifies the westward Saharan pathway as the optimal route for resolving TPSC-associated remote climate impacts.

To figure out TPSC-Saharan circulation linkages, we conduct two TPSC experiments using CESM (see Methods). When TPSC decreases (i.e., negative TPSC phase), the Tibetan Plateau functions as an anomalous atmospheric heat source (15–20 W m^{-2}; Figure 3a insert and Figure S10a in Supporting Information S1). This thermal forcing arises from enhanced terrain heating due to increased bare-ground exposure and moisture intrusion following TPSC reduction (Figure S9 in Supporting Information S1). Such intensified heating creates a robust thermal pump effect, drawing surrounding air masses into the Plateau's atmospheric column (Figure 3a). The convective updrafts subsequently drive significant easterly anomalies along the tropical easterly jet that penetrate the Saharan sector (Figure 3a).

Concurrently, an upper-level divergence anomaly over the Saharan Desert (Figure S11 in Supporting Information S1) induces pronounced dust updraft anomalies (Figure 3a; Figures S12a and S13c in Supporting Information S1). Driven by TPSC-associated easterly anomalies (Figure 3b; Figures S12d and S12e in Supporting Information S1), an accelerated tropical easterly jet and enhanced Saharan updraft anomalies create favorable dynamical conditions for dust mobilization (Figures S12a and S13c in Supporting Information S1). As the TPSC forcing persists into September, the tropical easterly jet further transports increased Saharan dust to the tropical Pacific (Figure S13 in Supporting Information S1). Therefore, TPSC reduction elevates dust concentrations in the tropical eastern Pacific by 1.2–1.6-fold relative to enhanced TPSC conditions (Figure S12b in Supporting Information S1).

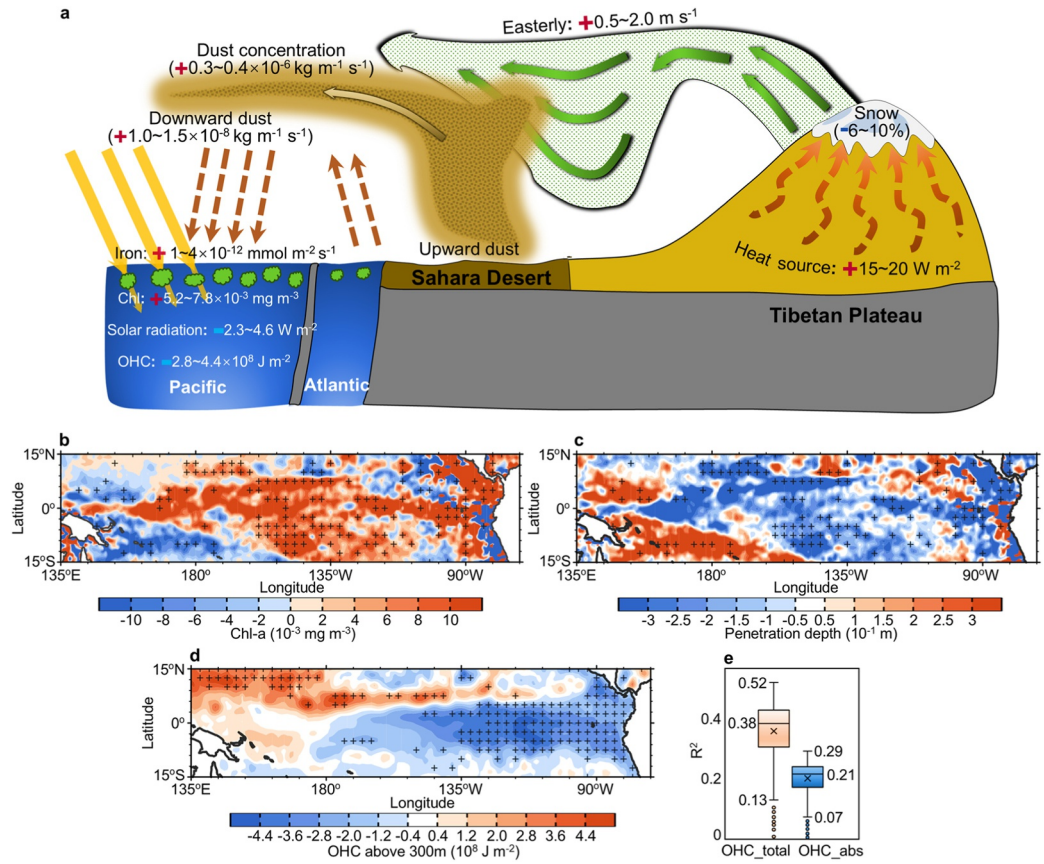

Figure 4. TPSC-driven Equatorial Pacific oceanic energy variations. (a) Conceptual diagram illustrates TPSC impact on the Equatorial Pacific dust-iron fertilization, biological response, and energetic variations. September anomalies of (b) MODIS surface chlorophyll-a concentration, (c) oceanic irradiance penetration depth, and (d) ORAS5 upper ocean heat content (above 300 m), shown as the partial regression onto -TPSC index (deep water upwelling impacts removed). Hatched areas: 95% statistical significance. (e) Coefficient of determination (R^2) between upper ocean heat content (OHC_total) in the Niño 3 region ($N = 671$) and the TPSC index, with absolute contribution (OHC_abs) estimated as the product of the OHC_total and the impact conversion factor.

Generally, the Equatorial Pacific constitutes a "high-nitrate, low-chlorophyll" (HNLC) region, primary due to strong upwelling of nitrate-rich deep water with limited micronutrient iron availability (Browning & Moore, 2023; Browning et al., 2023; Ustick et al., 2021; Westberry et al., 2023). Thus, dust deposition potentially plays an important role in stimulating productivity in these HNLC areas through dust-iron fertilization (Lamy et al., 2014; Letelier et al., 2019). Reduced TPSC increases dust loading and dust deposition anomalies in the eastern Equatorial Pacific (Figure 3c). This elevates the dust-derived iron flux anomalies (Figure 3d) and sea surface layer dissolved iron concentrations (Figure S14 in Supporting Information S1). Therefore, negative TPSC anomalies promote dust-mediated iron fertilization across the Equatorial Pacific.

3.3. Biogeochemical Mechanisms Impacting ENSO Variability

Persistent dust-derived iron fertilization linked to decreased TPSC during warm seasons could impact the enhanced phytoplankton accumulation in the central-eastern Equatorial Pacific. This is observed from September positive satellite chlorophyll-*a* anomalies (5.2–7.8 × 10^{-8} mg m^{-3}; Figure 4b). Making assumptions about the amount of enhanced dust-iron supply, phytoplankton iron requirements, and carbon: chlorophyll ratios, further indicate that TPSC-associated dust anomalies favor significant chlorophyll enhancement (Figure S15 in Supporting Information S1).

Phytoplankton blooms contribute to ocean mixed-layer warming through solar radiation absorption by phytoplankton pigments (Sun et al., 2021; R.-H. Zhang, 2015). However, these blooms also reduce penetration depth of

19448007, 2026, 6, Downloaded from https://agupubs.onlinelibrary.wiley.com/doi/10.1029/2025GL120206 by Chao Zhang - Xiamen University , Wiley Online Library on [14/03/2026]. See the Terms and Conditions (https://onlinelibrary.wiley.com/terms-and-conditions) on Wiley Online Library for rules of use; OA articles are governed by the applicable Creative Commons License

19448007, 2026, 6, Downloaded from https://agupubs.onlinelibrary.wiley.com/doi/10.1029/2025GL120206 by Chao Zhang - Xiamen University , Wiley Online Library on [14/03/2026]. See the Terms and Conditions (https://onlinelibrary.wiley.com/terms-and-conditions) on Wiley Online Library for rules of use; OA articles are governed by the applicable Creative Commons License

solar irradiance via light attenuation, cooling seawater within the upper thermocline (Kirk, 2011; Morel & Prieur, 1997). Increased phytoplankton biomass induces mixed-layer heating that peaks seasonally in early spring (~20°C month^{-1}) but declines markedly during summer and early autumn (~8°C month^{-1}; Figure S16a in Supporting Information S1). As such, September mixed layer heating associated with TPSC-driven phytoplankton enhancement is negligible (~0.6°C month^{-1}; Figure S16b in Supporting Information S1).

Conversely, increased phytoplankton abundance associated with TPSC reduction results in the penetration depth of solar irradiance deeper into the upper thermocline (Figure 4c). Such enhanced light attenuation significantly decreases seawater energy absorption at these greater depths. This potentially contributes to prominent negative upper-ocean (0–300 m) heat content anomalies ($-2.8 \sim -4.4 \times 10^8$ J m^{-2}; Figure 4d). Quantitative analysis using impact conversion factor shows that TPSC reduction contributes a 21% (7%–29%) decline in upper-ocean heat content (Figure 4e), establishing conducive conductive to La Niña development. Conversely, positive TPSC anomalies exert opposing effects, favoring El Niño occurrence.

The analysis above reveals biogeochemical mechanisms by which TPSC influences July-September ENSO occurrence. While ENSO negatively correlates with Equatorial Pacific surface chlorophyll, the biogeochemical processes exhibit significant phase-dependence across ENSO cycles (Lim et al., 2022; R.-H. Zhang, 2015). During La Niña mature/decaying phases, deep water upwelling iron sustains elevated phytoplankton biomass into the following spring, underscoring ENSO's dominant control on phytoplankton dynamics (Lim et al., 2022). However, the variations in chlorophyll are not synchronized with ENSO phases (Lim et al., 2022; Meehl et al., 2021). During ENSO onset period, about 79% of Equatorial Pacific chlorophyll responses precede SST changes by ~1.5 months (Park et al., 2018). This indicates non-upwelling iron sources gain importance when upwelling fails to deliver adequate iron during the ENSO transitional phase. Dust-derived iron supplies 30.0%–44.7% of eastern Equatorial Pacific iron during boreal summer (Park et al., 2018), highlighting its biogeochemical significance.

4. Summary and Discussions

This study reveals that anomalous TPSC, via biogeochemical pathways, contributes about one-quarter of ENSO variability, potentially modulating its development during July-September (Figure 4a). In a warming climate, the projected decline in TPSC may intensify this mechanism, potentially raising the frequency of La Niña events and amplifying associated extremes—a trend consistent with recent observations (Cai et al., 2015; Wang et al., 2023; Williams et al., 2020). Our work elucidates an important biogeochemical process in ENSO dynamics and underscores its implications for improving preparedness against future climate risks.

Although equatorial zonal wind anomalies impact ENSO dynamics through thermocline feedback, upwelling, and zonal currents (Cai et al., 2015; Wang et al., 2023), TPSC-induced phytoplankton changes also modulate upper-ocean energy via solar penetration depth. Notably, TPSC's impact on Niño 3 SST exhibits zonal asymmetry. Regressed negative SST anomalies span the central-eastern Equatorial Pacific, while information flow from TPSC to SST concentrates specifically in the eastern sector (Figure S17 in Supporting Information S1). Multi-regression analysis (see Methods in Supporting Information S1) identifies insignificant ocean heat content correlations with biogeochemical/physical processes in the western Niño 3 region ($r = 0.24$, $p > 0.05$), contrasting strong eastern correlation ($r = 0.49$, $p < 0.01$). Crucially, our multi-regression model indicates that solar penetration depth (50.2%) and zonal wind anomalies (49.8%) contribute equally to eastern upper ocean heat content variability, revealing their comparable dominant role in ENSO development.

In July, the TPSC exhibits a significant unidirectional information flow toward ENSO (Figure 1a), indicating its causal role in ENSO development. By August–September, a near-equivalent bidirectional information flow emerges (Figure 1a), suggesting that the developing ENSO also feeds back on TPSC variability. Composite analysis shows that after removing strong ENSO years, the La Niña signal weakens (Figure S7a in Supporting Information S1), underscoring that strong ENSO events may exert an influence on the TPSC.

Uncertainties remain in this study. The information flow analysis identifies directional dependence, but it cannot fully separate external forcing from ENSO' internal variability. Furthermore, the current model experiments, which employ fixed SSTs, preclude a direct assessment of ENSO sensitivity. Additionally, mechanistic understanding of the biogeochemical pathway, particularly the climate-system impacts of dust-derived bio-essential trace elements, phytoplankton growth dynamics, and light attenuation, requires deeper exploration.

Conflict of Interest

The authors declare no conflicts of interest relevant to this study.

Data Availability Statement

Data - All study data are publicly available. The NOAA satellite-derived snow cover data sets are sourced from Robinson et al. (2012). The MERRA-2 dust data sets are provided by Global Modeling and Assimilation Office (2015). Hadley Center SST data are provided by Rayner et al. (2003). The ORAS5 upper ocean heat content and mixed layer depth data sets are provided by Zuo et al. (2018). The ERA5 atmospheric reanalysis data sets are sourced from Hersbach et al. (2020). The NCEP–DOE-R2 atmospheric data sets are obtained from Kanamitsu et al. (2002). The Mercator-Ocean dissolved iron data sets are provided by Global Ocean Biogeochemistry Hindcast (2024).

Software - Data processing preformed using MATLAB and Intel® Fortran Compiler. Fortran codes for regression and filtering can be accessed through Zendo and provided by C. Zhang (2025). MATLAB codes for information flow analysis are available at http://www.ncoads.cn/article/show/63.aspx.

Acknowledgments

The authors would like to express their sincere thanks to Prof. X. San Liang (Fudan University, Shanghai, China) for providing the LKIF method, Prof. Jakob Runge (Institut für Datenwissenschaften, Jena, Germany) for supplying the PCMCI method, and Dr. Yuhen Tang (Nanjing University of Information Science and Technology, Nanjing, China) for technical support. C.Z., T.B., and E.P.A. thank the Helmholtz Centre for Ocean Research Kiel for their support. We acknowledge NASA's Ocean Biology Distributes Active Archive Center (OB.DAAC) for the satellite-derived chlorophyll-*a* data. This research was funded by the National Natural Science Foundation of China Grants 42305016 (to C.Z.) and 42030602 (to A.D.). C.Z. also acknowledges financial support from the Chinese Scholarship Council (File No. 202306310194) and the Outstanding Postdoctoral Scholarship provided by the State Key Laboratory of Marine Environmental Science at Xiamen University.

References

Browning, T. J., & Moore, C. M. (2023). Global analysis of ocean phytoplankton nutrient limitation reveals high prevalence of co-limitation. *Nature Communications*, *14*(1), 5014. https://doi.org/10.1038/s41467-023-40774-0

Browning, T. J., Saito, M. A., Garaba, S. P., Wang, X., Achterberg, E. P., Moore, C. M., et al. (2023). Persistent equatorial Pacific iron limitation under ENSO forcing. *Nature*, *621*(7978), 330–335. https://doi.org/10.1038/s41586-023-06439-0

Cai, W., Wang, G., Santoso, A., McPhaden, M. J., Wu, L., Jin, F. F., et al. (2015). Increased frequency of extreme La Niña events under greenhouse warming. *Nature Climate Change*, *5*(2), 132–137. https://doi.org/10.1038/nclimate2492

Cohen, J., Agel, L., Barlow, M., Garfinkel, C. I., & White, I. (2021). Linking Arctic variability and change with extreme winter weather in the United States. *Science*, *373*(6559), 1116–1121. https://doi.org/10.1126/science.abi9167

Global Modeling and Assimilation Office (GMAO). (2015). *MERRA-2 tavgM_2d_aer_Nx: 2d, monthly mean, time-averaged, single-Level, assimilation, aerosol diagnostics V5.12.4, Greenbelt, MD, USA*. Goddard Earth Sciences Data and Information Services Center (GES DISC). https://doi.org/10.5067/FH9A0MLJPC7N

Global Ocean Biogeochemistry Hindcast. (2024). E.U. Copernicus Marine Service Information (CMEMS). *Marine Data Store (MDS)*. https://doi.org/10.48670/moi-00019

Henderson, G., Peings, Y., Furtado, J., & Kushner, P. (2018). Snow–atmosphere coupling in the Northern Hemisphere. *Nature Climate Change*, *8*(11), 954–963. https://doi.org/10.1038/s41558-018-0295-6

Hersbach, H., Bell, B., Berrisford, P., Hirahara, S., Horányi, A., Muñoz-Sabater, J., et al. (2020). The ERA5 global reanalysis. *Quarterly Journal of the Royal Meteorological Society*, *146*(730), 1999–2049. https://doi.org/10.1002/qj.3803

Huang, J., Zhou, X., Wu, G., Xu, X., Zhao, Q., Liu, Y., et al. (2023). Global climate impacts of land-surface and atmospheric processes over the Tibetan Plateau. *Reviews of Geophysics*, *61*(3), e2022RG000771. https://doi.org/10.1029/2022RG000771

Jiang, X., Zhang, T., Tam, C.-Y., Chen, J., Lau, N.-C., Yang, S., & Wang, Z. (2019). Impacts of ENSO and IOD on snow depth over the Tibetan Plateau: Roles of convections over the western North Pacific and Indian Ocean. *Journal of Geophysical Research: Atmospheres*, *124*(22), 11961–11975. https://doi.org/10.1029/2019JD031384

Kanamitsu, M., Ebisuzaki, W., Woollen, J., Yang, S.-K., Hnilo, J., Mg, F., & Potter, G. (2002). NCEP-DOE AMIP-II reanalysis (R-2). *Bulletin of the American Meteorological Society*, *83*(11), 1631–1643. https://doi.org/10.1175/Bams-83-11-1631

Kirk, J. T. O. (2011). *Light and photosynthesis in aquatic ecosystems*. Cambridge University Press.

Krishnamurthy, A., Moore, J. K., Mahowald, N. M., Luo, C., & Zender, C. S. (2010). Impacts of atmospheric nutrient inputs on marine biogeochemistry. *Journal of Geophysical Research: Biogeoscience*, *115*(G1), G01006. https://doi.org/10.1029/2009JG001115

Lamy, F., Gersonde, R., Winckler, G., Esper, O., Jaeschke, A., Kuhn, G., et al. (2014). Increased dust deposition in the Pacific southern ocean during glacial periods. *Science*, *343*(6169), 403–407. https://doi.org/10.1126/science.1245424

Lawrence, D. M., Oleson, K. W., Flanner, M. G., Fletcher, C. G., Lawrence, P. J., Levis, S., et al. (2012). The CCSM4 land simulation, 1850–2005: Assessment of surface climate and new capabilities. *Journal of Climate*, *25*(7), 2240–2260. https://doi.org/10.1175/JCLI-D-11-00103.1

Letelier, R. M., Björkman, K. M., Church, M. J., Hamilton, D. S., Mahowald, N. M., Scanza, R. A., et al. (2019). Climate-driven oscillation of phosphorus and iron limitation in the North Pacific Subtropical Gyre. *Proceedings of the National Academy of Sciences of the United States of America*, *116*(26), 12720–12728. https://doi.org/10.1073/pnas.1900789116

Li, W., Guo, W., Qiu, B., Xue, Y., Hsu, P.-C., & Wei, J. (2018). Influence of Tibetan Plateau snow cover on East Asian atmospheric circulation at medium-range time scales. *Nature Communications*, *9*(1), 4243. https://doi.org/10.1038/s41467-018-06762-5

Li, X., Zhang, Y., Hou, J., Wang, M., Fan, B., Yan, J., et al. (2022). Spatio-temporal patterns of centennial-scale climate change over the Tibetan Plateau during the past two millennia and their possible mechanisms. *Quaternary Science Reviews*, *292*, 107664. https://doi.org/10.1016/j.quascirev.2022.107664

Li, Y., Xu, F., Wan, L., Chen, P., Guo, D., Chang, S., & Yang, C. (2023). Effect of ENSO on the ozone valley over the Tibetan Plateau based on the WACCM4 Model. *Remote Sensing*, *15*(2), 525. https://doi.org/10.3390/rs15020525

Li, Z., Sun, D., Wang, S., Huan, Y., Zhang, H., Yuan, Y., & He, Y. (2024). Ocean-scale patterns of environment and climate changes driving global marine phytoplankton biomass dynamics. *Science Advances*, *10*(45), eadm7556. https://doi.org/10.1126/sciadv.adm7556

Liang, X. S. (2016). Information flow and causality as rigorous notions ab initio. *Physical Review*, *94*(5), 052201. https://doi.org/10.1103/PhysRevE.94.052201

Liang, X. S., & Kleeman, R. (2005). Information transfer between dynamical system components. *Physical Review Letters*, *95*(24), 244101. https://doi.org/10.1103/PhysRevLett.95.244101

19448007, 2026, 6, Downloaded from https://agupubs.onlinelibrary.wiley.com/doi/10.1029/2025GL120206 by Chao Zhang - Xiamen University , Wiley Online Library on [14/03/2026]. See the Terms and Conditions (https://onlinelibrary.wiley.com/terms-and-conditions) on Wiley Online Library for rules of use; OA articles are governed by the applicable Creative Commons License

Lim, H.-G., Dunne, J. P., Stock, C. A., Ginoux, P., John, J. G., & Krasting, J. (2022). Oceanic and atmospheric drivers of post-El-Niño chlorophyll rebound in the equatorial Pacific. *Geophysical Research Letters*, *49*(5), e2021GL096113. https://doi.org/10.1029/2021GL096113

Liu, S., Wu, Q., Yao, Y., Schroeder, S., & Wang, L. (2022). Impacts of autumn-winter Tibetan Plateau snow anomalies on North Atlantic-Europe and Arctic climate. *Journal of Geophysical Research: Atmospheres*, *127*(12), e2021JD035791. https://doi.org/10.1029/2021JD035791

Luo, C., Mahowald, N., Bond, T., Chuang, P. Y., Artaxo, P., Siefert, R., et al. (2008). Combustion iron distribution and deposition. *Global Biogeochemical Cycles*, *22*(1), GB1012. https://doi.org/10.1029/2007GB002964

Mahowald, N. M., Engelstaedter, S., Luo, C., Sealy, A., Artaxo, P., Benitez-Nelson, C., et al. (2009). Atmospheric iron deposition: Global distribution, variability, and human perturbations. *Annual Review of Marine Science*, *1*, 245–278. https://doi.org/10.1146/annurev.marine.010908.163727

Mahowald, N. M., Hamilton, D. S., Mackey, K. R. M., Moore, J. K., Baker, A. R., Scanza, R. A., & Zhang, Y. (2018). Aerosol trace metal leaching and impacts on marine microorganisms. *Nature Communications*, *9*(1), 2614. https://doi.org/10.1038/s41467-018-04970-7

Matsui, H., Mahowald, N. M., Moteki, N., Hamilton, D. S., Ohata, S., Yoshida, A., et al. (2018). Anthropogenic combustion iron as a complex climate forcer. *Nature Communications*, *9*(1), 1593. https://doi.org/10.1038/s41467-018-03997-0

Meehl, G. A., Richter, J. H., Teng, H., Capotondi, A., Cobb, K., Doblas-Reyes, F., et al. (2021). Initialized Earth System prediction from subseasonal to decadal timescales. *Nature Reviews Earth & Environment*, *2*(5), 340–357. https://doi.org/10.1038/s43017-021-00155-x

Morel, A., & Prieur, L. (1977). Analysis of variations in ocean color. *Limnology & Oceanography*, *4*, 709–722. https://doi.org/10.4319/lo.1977.22.4.0709

Murtugudde, R., Beauchamp, J., McClain, C. R., Lewis, M., & Busalacchi, A. J. (2002). Effects of penetrative radiation on the upper tropical ocean circulation. *Journal of Climate*, *15*(5), 470–486. https://doi.org/10.1175/1520-0442(2002)015<0470:EOPROT>2.0.CO;2

Park, J. Y., Dunne, J. P., & Stock, C. A. (2018). Ocean chlorophyll as a precursor of ENSO: An Earth system modeling study. *Geophysical Research Letters*, *45*(4), 1939–1947. https://doi.org/10.1002/2017GL076077

Park, S., Bretherton, C. S., & Rasch, P. J. (2014). Integrating cloud processes in the community atmosphere model, version 5. *Journal of Climate*, *27*(18), 6821–6856. https://doi.org/10.1175/JCLI-D-14-00087.1

Rayner, N. A., Parker, D., Horton, E. B., Folland, C., Alexander, L., Rowell, D., et al. (2003). Global analyses of sea surface temperature, sea ice, and night marine air temperature since the late Nineteenth Century. *Journal of Geophysical Research*, *108*(D14), 4407. https://doi.org/10.1029/2002JD002670

Robinson, D. A., Estilow, T. W., & Program, N. C. (2012). *NOAA Climate Data Record (CDR) of Northern Hemisphere (NH) Snow Cover Extent (SCE), version 1 [NCDC: C00756]*. NOAA National Centers for Environmental Information. https://doi.org/10.7289/V5N014G9

Scaife, A. A., Dunstone, N., Hardiman, S., Ineson, S., Li, C., Lu, R., et al. (2024). ENSO affects the North Atlantic Oscillation 1 year later. *Science*, *386*(6717), 82–86. https://doi.org/10.1126/science.adk4671

Shaman, J., & Tziperman, E. (2005). The effect of ENSO on Tibetan Plateau snow depth: A stationary wave teleconnection mechanism and implications for the South Asian monsoons. *Journal of Climate*, *18*(12), 2067–2079. https://doi.org/10.1175/JCLI3391.1

Sun, D., Fan, J., Wang, S., Zhang, H., Shen, X., Yuan, Y., & He, Y. (2021). Understanding optical absorption associated with phytoplanktonic groups in the marginal seas. *Science of the Total Environment*, *789*, 147846. https://doi.org/10.1016/j.scitotenv.2021.147846

Tziperman, E., Stone, L., Cane, M. A., & Jarosh, H. (1994). El Niño Chaos: Overlapping of resonances between the seasonal cycle and the Pacific ocean-atmosphere oscillator. *Science*, *264*(5155), 72–74. https://doi.org/10.1126/science.264.5155.72

Ustick, L. J., Larkin, A. A., Garcia, C. A., Garcia, N. S., Brock, M. L., Lee, J. A., et al. (2021). Metagenomic analysis reveals global-scale patterns of ocean nutrient limitation. *Science*, *372*(6539), 287–291. https://doi.org/10.1126/science.abe6301

Wang, B., Sun, W., Jin, C., Luo, X., Yang, Y. M., Li, T., et al. (2023). Understanding the recent increase in multiyear La Niñas. *Nature Climate Change*, *13*(10), 1075–1081. https://doi.org/10.1038/s41558-023-01801-6

Wang, R., Ren, H.-L., Liu, M., Zhou, F., & Du, J. (2024). Impact of the central-Pacific ENSO on the Tibetan Plateau precipitation in boreal spring. *Environmental Research Communications*, *6*(10), 101008. https://doi.org/10.1088/2515-7620/ad810d

Wen, Q., Döös, K., Lu, Z., Han, Z., & Yang, H. (2020). Investigating the role of the Tibetan Plateau in ENSO variability. *Journal of Climate*, *33*(11), 4835–4852. https://doi.org/10.1175/JCLI-D-19-0422.1

Westberry, T., Behrenfeld, M., Shi, Y., Yu, H., Remer, L., & Bian, H. (2023). Atmospheric nourishment of global ocean ecosystems. *Science*, *380*(6644), 515–519. https://doi.org/10.1126/science.abq5252

Williams, A. P., Cook, E. R., Smerdon, J. E., Cook, B. I., Abatzoglou, J. T., Bolles, K., et al. (2020). Large contribution from anthropogenic warming to an emerging North American megadrought. *Science*, *368*(6488), 314–318. https://doi.org/10.1126/science.aaz9600

Wu, C., Liu, G., Cong, L., Li, X., Liu, X., Liu, Y., et al. (2024). ENSO-driven hydroclimate changes in central Tibetan Plateau since middle Holocene: Evidence from Zhari Namco's lake sediments. *Quaternary Science Reviews*, *330*, 108593. https://doi.org/10.1016/j.quascirev.2024.108593

Wu, G., Duan, A., Liu, Y., Mao, J., Ren, R., Bao, Q., et al. (2014). Tibetan Plateau climate dynamics: Recent research progress and outlook. *National Science Review*, *2*(1), 100–116. https://doi.org/10.1093/nsr/nwu045

Wu, Q., Hu, H., & Zhang, L. (2011). Observed influences of autumn–early winter Eurasian snow cover anomalies on the hemispheric PNA-like variability in winter. *Journal of Climate*, *24*(7), 2017–2023. https://doi.org/10.1175/2011JCLI4236.1

Xiao, Z., & Duan, A. (2016). Impacts of Tibetan Plateau snow cover on the interannual variability of the East Asian summer monsoon. *Journal of Climate*, *29*(23), 8495–8514. https://doi.org/10.1175/JCLI-D-16-0029.1

Yi, B., & Bose, S. (2022). Quantum Liang information flow as causation quantifier. *Physical Review Letters*, *129*(2), 020501. https://doi.org/10.1103/PhysRevLett.129.020501

Yu, W., Liu, Y., Xu, L., Wu, G., Yang, S., Chen, D., et al. (2022). Potential impact of spring thermal forcing over the Tibetan Plateau on the following winter El Niño–Southern Oscillation. *Geophysical Research Letters*, *49*(6), e2021GL097234. https://doi.org/10.1029/2021GL097234

Yu, W., Liu, Y., Zhang, T., Yang, S., Wu, G., Chen, D., et al. (2023). Potential impact of winter–spring North Atlantic tripole SSTAs on the following autumn–winter El Nino–Southern Oscillation: Bridging role of the Tibetan Plateau. *Geophysical Research Letters*, *50*(5), e2022GL100663. https://doi.org/10.1029/2022GL100663

Zhang, C. (2025). Fortran codes for regression analysis and wave filtering used in the study "Influence of Tibetan Plateau snow cover on ENSO variability". *Zenodo*. https://doi.org/10.5281/zenodo.17042055

Zhang, C., Duan, A., Jia, X., & Liu, S. (2025). Connecting Tibetan Plateau snow change with Arctic sea-ice. *Geophysical Research Letters*, *52*(14), e2025GL116351. https://doi.org/10.1029/2025GL116351

Zhang, C., Duan, A., Jia, X., Wang, Z., & Pan, Z. (2023). A dynamic link between spring Arctic sea ice and the Tibetan Plateau snow increment indicator. *npj Climate and Atmospheric Science*, *6*(1), 191. https://doi.org/10.1038/s41612-023-00505-0

19448007, 2026, 6, Downloaded from https://agupubs.onlinelibrary.wiley.com/doi/10.1029/2025GL120206 by Chao Zhang - Xiamen University , Wiley Online Library on [14/03/2026]. See the Terms and Conditions (https://onlinelibrary.wiley.com/terms-and-conditions) on Wiley Online Library for rules of use; OA articles are governed by the applicable Creative Commons License

Zhang, C., & Jia, X. (2022). The seasonal evolution of the Tibetan Plateau snow cover related moisture during spring-to-summer. *Journal of Geophysical Research: Atmospheres*, *127*(11), e2022JD036560. https://doi.org/10.1029/2022JD036560

Zhang, C., Jia, X., & Wen, Z. (2021). Increased impact of the Tibetan Plateau spring snow cover to the Mei-yu rainfall over the Yangtze River Valley after the 1990s. *Journal of Climate*, *34*(14), 5985–5997. https://doi.org/10.1175/jcli-d-21-0009.1

Zhang, R.-H. (2015). Structure and effect of ocean biology-induced heating (OBH) in the tropical Pacific, diagnosed from a hybrid coupled model simulation. *Climate Dynamics*, *44*(3), 695–715. https://doi.org/10.1007/s00382-014-2231-4

Zhao, S., Jin, F.-F., Stuecker, M. F., Thompson, P. R., Kug, J.-S., McPhaden, M. J., et al. (2024). Explainable El Niño predictability from climate mode interactions. *Nature*, *630*(8018), 891–898. https://doi.org/10.1038/s41586-024-07534-6

Zuo, H., Balmaseda, M. A., Mogensen, K., & Tietsche, S. (2018). *OCEAN5: The ECMWF ocean reanalysis system and its real-time analysis component*. European Centre for Medium-Range Weather Forecasts. https://doi.org/10.21957/la2v0442

References From the Supporting Information

Jia, X., Zhang, C., Wu, R., & Qian, Q. (2021). Influence of Tibetan Plateau autumn snow cover on interannual variations in spring precipitation over southern China. *Climate Dynamics*, *56*(3–4), 767–782. https://doi.org/10.1007/s00382-020-05497-8

Krich, C., Runge, J., Miralles, D. F., Migliavacca, M., Perez-Priego, O., El-Madany, T., et al. (2020). Estimating causal networks in biosphere–atmosphere interaction with the PCMCI approach. *Biogeosciences*, *17*(4), 1033–1061. https://doi.org/10.5194/bg-17-1033-2020

Runge, J., Nowack, P., Kretschmer, M., Flaxman, S., & Sejdinovic, D. (2019). Detecting and quantifying causal associations in large nonlinear time series datasets. *Science Advances*, *5*(11), eaau4996. https://doi.org/10.1126/sciadv.aau4996

Runge, J., Gerhardus, A., Varando, G., Eyring, V., & Camps-Valls, G. (2023). Causal inference for time series. *Nature Reviews Earth & Environment*, *4*(7), 487–505. https://doi.org/10.1038/s43017-023-00431-y

Spirtes, P., Glymour, C., & Scheines, R. (2000). *Causation, prediction, and search*. MIT Press.

Yanai, M., Esbensen, S., & Chu, J.-H. (1973). Determination of bulk properties of tropical cloud clusters from large-scale heat and moisture budgets. *Journal of the Atmospheric Sciences*, *30*(4), 611–627. https://doi.org/10.1175/1520-0469(1973)030<0611:DOBPOT>2.0.CO;2

Yu, W., Liu, Y., Yang, X., Wu, G., He, B., Li, J., & Bao, Q. (2021). Impact of North Atlantic SST and Tibetan Plateau forcing on seasonal transition of springtime South Asian monsoon circulation. *Climate Dynamics*, *56*(1–2), 559–579. https://doi.org/10.1007/s00382-020-05491-0

Zhang, C., Duan, A., Jia, X., Hu, J., & Liu, S. (2023). Snow cover on the Tibetan Plateau and Lake Baikal intensifies the Winter North Atlantic Oscillation. *Geophysical Research Letters*, *50*(16), e2023GL104754. https://doi.org/10.1029/2023GL104754

Zhang, C., & Duan, A. (2026). Reversal of the Tibetan snow-India Burma trough relationship. *npj Climate and Atmospheric Science*, *9*(1), 26. https://doi.org/10.1038/s41612-025-01301-8

Zhang, C., Guo, Y., & Wen, Z. (2022). Interdecadal change in the effect of Tibetan Plateau snow cover on spring precipitation over Eastern China around the early 1990s. *Climate Dynamics*, *58*(9–10), 2807–2824. https://doi.org/10.1007/s00382-021-06035-w

19448007, 2026, 6, Downloaded from https://agupubs.onlinelibrary.wiley.com/doi/10.1029/2025GL120206 by Chao Zhang - Xiamen University , Wiley Online Library on [14/03/2026]. See the Terms and Conditions (https://onlinelibrary.wiley.com/terms-and-conditions) on Wiley Online Library for rules of use; OA articles are governed by the applicable Creative Commons License